

Key Points:

- Grooves on a laboratory fault are generated by detached particles and gouge clumps (third-body wear)
- Groove density increases systematically with normal stress in the experiment
- At stresses higher than 20 MPa, grooves coalesce into a qualitatively different, corrugated morphology

Supporting Information:

- Supporting Information S1
- Original Version of Manuscript
- Peer Review History
- Authors' Response to Peer Review Comments
- First Revision of Manuscript
- Authors' Response to Peer Review Comments
- Second Revision of Manuscript [Accepted]

Correspondence to:

E. E. Brodsky,
brodsky@ucsc.edu

Citation:

Brodsky, E. E., McLaskey, G. C., & Ke, C.-Y. (2020). Groove generation and coalescence on a large-scale laboratory fault. *AGU Advances*, 1, e2020AV000184. <https://doi.org/10.1029/2020AV000184>

Received 23 MAR 2020

Accepted 17 AUG 2020

The peer review history for this article is available as a PDF in the Supporting Information.

©2020. The Authors.

This is an open access article under the terms of the Creative Commons Attribution-NonCommercial License, which permits use, distribution and reproduction in any medium, provided the original work is properly cited and is not used for commercial purposes.

Groove Generation and Coalescence on a Large-Scale Laboratory Fault

Emily E. Brodsky¹ , Gregory C. McLaskey² , and Chun-Yu Ke² 

¹Department of Earth and Planetary Sciences, University of California, Santa Cruz, CA, USA, ²Department of Civil and Environmental Engineering, Cornell University, Ithaca, NY, USA

Abstract Faults are the products of wear processes acting at a range of scales from nanometers to kilometers. Grooves produced by wear are a first-order observable feature of preserved surfaces. However, their interpretation is limited by the complex geological histories of natural faults. Here we explore wear processes on faults by forensically examining a large-scale controlled, laboratory fault which has a maximum offset between the sides of 42 mm and has been reset multiple times for a cumulative slip of approximately 140 mm. We find that on both sides of the fault scratches are formed with lengths that are longer than the maximum offset but less than the cumulative slip. The grooves are explained as a result of interaction with detached gouge rather than as toolmarks produced by an intact protrusion on one side of the fault. The density of grooves increases with normal stress. The experiment has a range of stress of 1–20 MPa and shows a density of 10 grooves/m/MPa in this range. This value is consistent with recent inferences of stress-dependent earthquake fracture energy of 0.2 J/m²/MPa. At normal stresses above 20 MPa, the grooves are likely to coalesce into a corrugated surface that more closely resembles mature faults. Groove density therefore appears to be an attractive target for field studies aiming to determine the distribution of normal stress on faults. At low stresses the groove spacing can be measured and contrasted with areas where high stresses produce a corrugated surface.

Plain Language Summary The surfaces of faults have grooves that hold information about the fault's mechanics and history. Interpreting these grooves on a complex fault needs to be guided by models of simpler systems; however, such models must also be sufficiently large to capture the multiscale processes carving the fault surface. Here we perform experiments on a 3-m-long artificial fault in a laboratory setting and find that the fault surface develops roughness during slip. First, small particles break off in between the surfaces and excavate grooves on each side. These grooves are created by detached particles rather than protrusions attached to one side or the other. As the normal stress between the fault sides increases, so does the groove density. In a region of the laboratory fault where the normal stress is high, the grooves coalesce to form a corrugated surface that appears more like a natural fault than the other experimentally created surfaces. The work both gives insight into roughness formation and suggests a strategy for future field work that could use roughness to map normal stress variations.

1. Introduction

Geological observations of faults can identify the final products of failure on slip surfaces. Significant effort has gone into forensically connecting specific surficial features to geological processes; however, most of those observations are on faults with complex geological history (e.g., Brodsky et al., 2016; Doblas, 1998; Engelder, 1974; Kirkpatrick & Rowe, 2013; Rowe & Griffith, 2015). Laboratory experiments play a key role in helping link-specific features such as striations, polish, and gouge formation to their underlying processes (Means, 1987; Renard et al., 2012; Fondriest et al., 2013; Tisato et al., 2012; Toy et al., 2017). However, most laboratory experiments focused on wear products have been limited to relatively small-scale samples (Badt et al., 2016; Boneh & Reches, 2018; Davidesko et al., 2014; Hirose et al., 2012). This is a particularly serious problem for fault wear because the process is intrinsically multiscale with the interactions between micron-scale asperities and millimeter-sized grains resulting in observable features at centimeter or meter scale (Yamashita et al., 2015). While small-scale experiments focus on isolating specific friction and wear behavior, only large-scale experiments can capture the spatial distribution of wear features, their density, and their interactions as a function of variables such as normal stress and displacement.

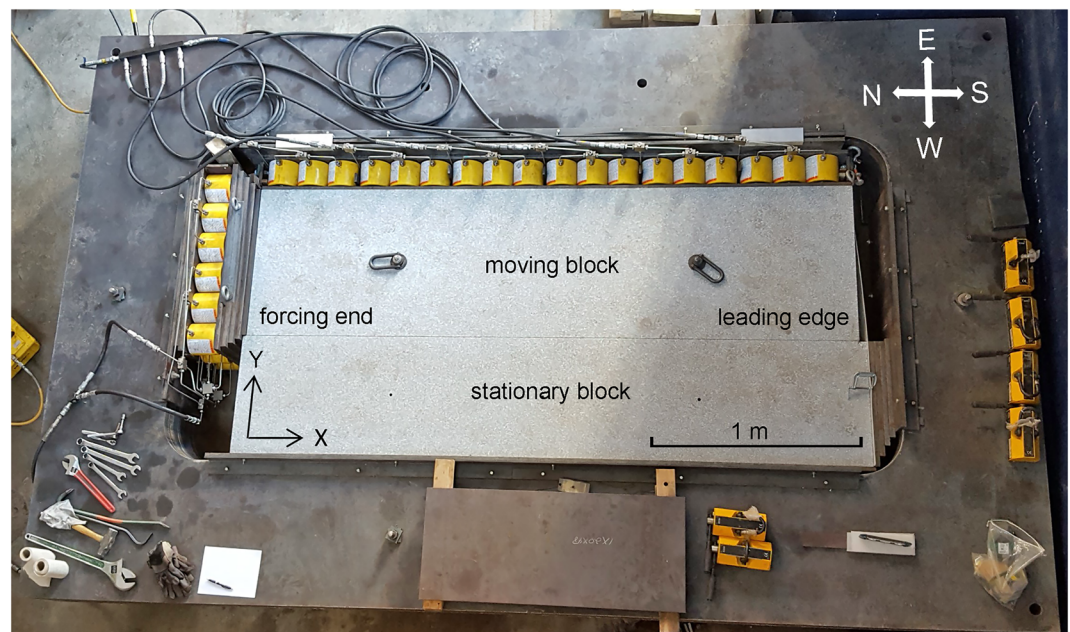


Figure 1. Photograph of the Cornell 3 m apparatus. The Barre gray granite sample consists of a moving block and stationary block whose interface forms the laboratory fault. Normal and shear stress is applied to the fault via arrays of 36 and 18 hydraulic cylinders that apply force to the top and left sides of the moving block, respectively.

To meet this need, we have capitalized on the Cornell 3 m apparatus. This machine loads a 3 m granite sample, and deformation occurs on a $3.1 \text{ m} \times 0.3 \text{ m}$ granite/granite simulated fault (Ke et al., 2018; McLaskey, 2019; Wu & McLaskey, 2019). This sample has been in use for 2.5 years and has hosted hundreds of slip events on the surface for a total of about 140 mm of fault slip at 1–12 MPa sample-average normal stress levels (see supporting information Table S1). In this study, we separated the blocks and mapped the wear features on the fault surfaces. After reviewing our strategy for mapping the many grooves and smears that were visible on the fault surfaces, we enumerate six key observations that cumulatively demonstrate that the grooves are formed by detached particles etching the surface in a process that is significantly affected by the local normal stress regimes. This grooving by a detached particle is known in the engineering literature as third-body wear (e.g., Godet, 1984), and it produces wear marks that are not equivalent to toolmarks produced by a fixed protrusion on one side of the wall. The observations emphasize the importance of third-body wear in determining the steady-state geometry of faults and suggest a strategy for field studies to explore normal stress variations in situ.

Throughout this study we refer to trenches formed in the fault surfaces as grooves, rather than striations, slickenlines, or another term. Geological nomenclature of fault surface features is extensively reviewed by Doblas (1998). The term striation is specifically defined by Toy et al. (2017) as a groove formed as a consequence of brittle wear. Although we will eventually infer a third-body wear origin for the grooves observed here, we have no direct evidence of their brittle nature and thus prefer the nongenetic term groove.

2. Mapping Study

The Cornell 3 m apparatus is a biaxial direct shear device that applies force to two 3-m-long granite blocks, shown in Figure 1. The moving block is pushed past the stationary block with hydraulic pistons. There is an intrinsic asymmetry to the device as the pistons act on only one side of the moving block. Thus, we refer to the “leading edge” and “forcing end” to distinguish the boundary conditions at each end of the simulated fault (Figure 1). The blocks were originally cut and prepared by the manufacturer to be flat to $125 \mu\text{m}$ before assembly. After the initial 1 mm of slip, the fault surfaces were inspected, and a fine layer of rock powder was observed throughout the $3.1 \text{ m} \times 0.3 \text{ m}$ simulated fault. After 18 mm of cumulative slip the sample was opened a second time and the gouge was wiped off. The fault had been visibly polished, as evidenced by its enhanced ability to reflect light relative to a section of the simulated fault that was not worn because it was mated against a trough on the opposite side of the fault (red in the wear map in Figure 2, described

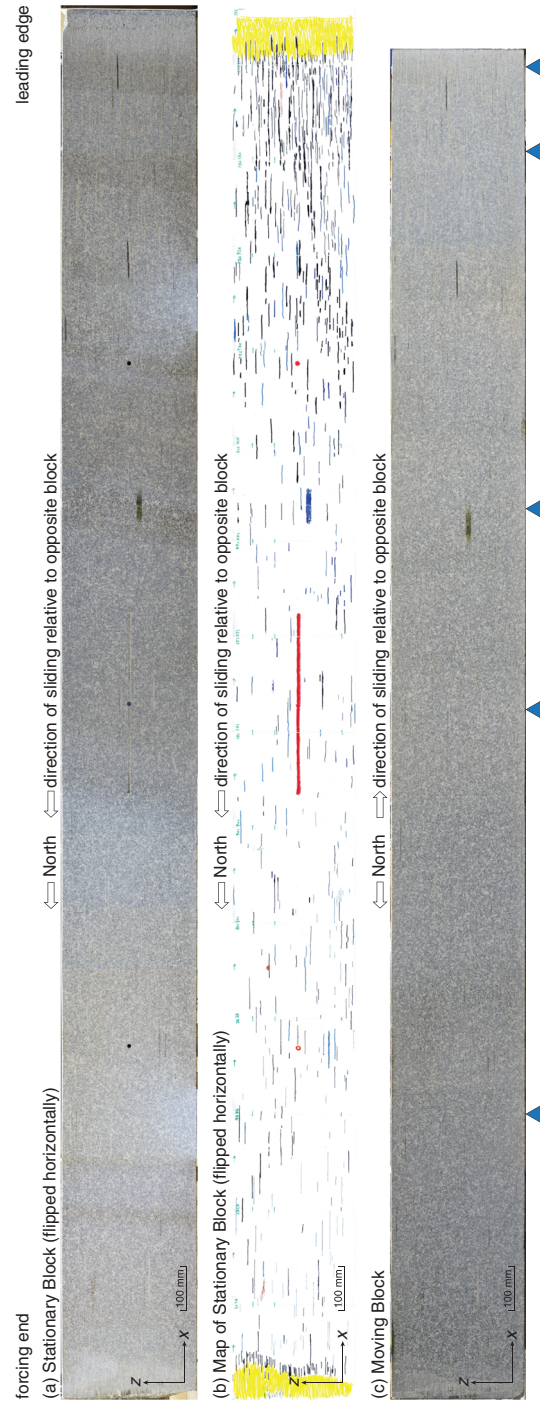


Figure 2. Photographs of worm sides of the fault and map of roughness measurements shown in Figure 6. Yellow regions are worn with overlapping grooves so dense that individual grooves were not mapped. Note panels (a) and (b) have been flipped horizontally to illustrate the mirror image match with the moving block.

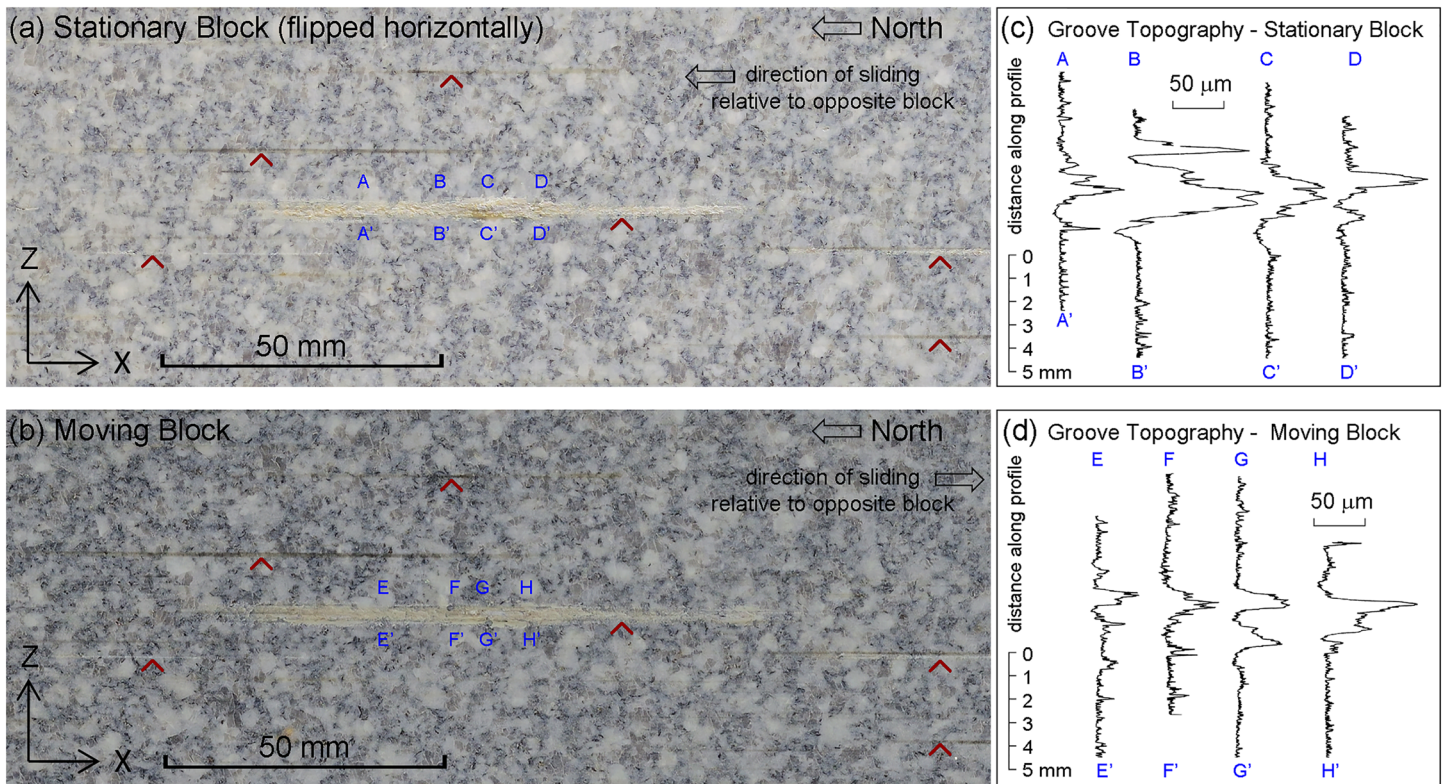


Figure 3. Example of mirror image grooves. Annotated photographs of the fault surface of the stationary block (a) and moving block (b) depict a particularly large groove at $x \sim 350$ mm. Red annotations show directly that each groove and smear has a corresponding groove on the opposite side of similar scale. Blue letters denote the locations of topography measurements shown in (c) and (d). The profiles, taken after the gouge was removed, show this large groove which is 50–100 mm deep and was carved on both sides of the fault.

below). Thenceforth, gouge was preserved. After sets of experiments totaling 15–42 mm of displacement, the cylinders were retracted and the moving block was reset with an overhead crane to its original position relative to the stationary block (to 500 μm accuracy in the north-south direction and ~ 20 μm accuracy in the up-down direction), while fault surfaces were kept as undisturbed as possible. Since the installation of the experiment, the fault blocks were moved to their total possible displacement of about 42 mm twice, and were reset multiple times prior to the mapping study described below (see supporting information Table S1).

We mapped the fault surface on the stationary block by overlaying transparencies onto the surface and tracing all visible wear features. This standard geological mapping technique (e.g., Graham et al., 2003) is more applicable to the large-scale blocks with low amplitude roughness than LiDAR or structure from motion photogrammetry techniques, both of which lack the resolution to efficiently cover the surface. Grooves on the fault surface (typically light colored due to the light colored gouge powder associated with them) were marked in black. Smeared minerals (typically dark colored or nearly black) were marked in blue. Sections that were too heavily worn to count individual grooves were colored yellow. The locations of injection ports and troughs for planned fluid injection experiments were colored red.

Orientation is a confusing aspect of this study. The maps were constructed facing each side of the block, and thus the left-hand side of the map is the leading edge on the stationary-block side of the fault and the forcing end on the moving-block side of the fault. We therefore reference cardinal directions in this mapping study (see compass on Figure 1) and flipped both the maps and the photographs of the stationary block in the N-S direction to compare them to the moving block with north on the left-hand side of both images. (This flipping procedure is a reflection about a vertical line halfway between the forcing and leading edges.) In this reference frame, we found the moving and stationary blocks to be well matched (Figures 2 and 3). We then digitized these maps using a scanner (300 dpi resolution) for later

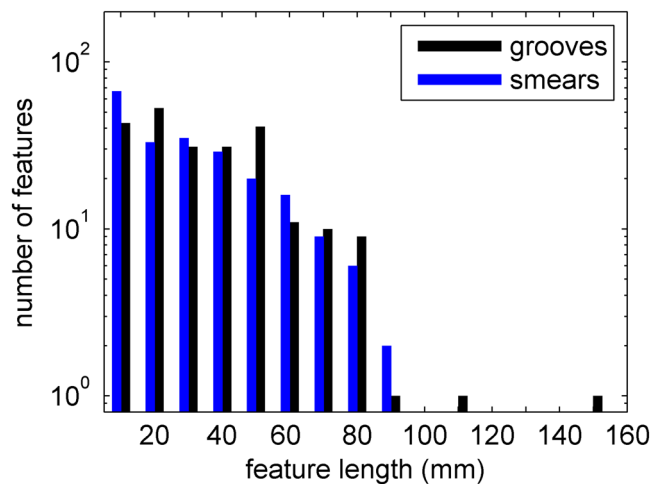


Figure 4. Distribution of lengths of mapped grooves and smears. Only mapped wear features between $x = 0.1$ m and $x = 2.81$ m were included since high groove density close to the ends of the samples made accurate counting impossible. Grooves longer than 90 mm are rare and likely indicate two grooves that merged.

processing. Figure 2 shows this map alongside panoramic photographs of the two sides of the fault surfaces.

The mapping data are complemented by measurements of fault roughness using a contact stylus profilometer (Mitutoyo Surftest SJ-210). We also compared the observed wear to the along-fault stress distribution determined from strain gages and a finite element model, as reported in Ke et al. (2018), and to the history and spatial distribution of fault slip failure modes on the sample.

3. Observations

3.1. The Relationship Between Opposing Sides of the Fault

The first and clearest observation is that wear marks on the opposite sides of the fault match. When the wear map was transferred to the opposite face of the fault, it was found that nearly all of the grooves and smears that were mapped on the stationary-block side of the fault had mirror image counterparts on the moving-block side of the fault. The match is clear both at the large scale (Figure 2) and at the level of individual scratches and smears, as shown in Figure 3. A positive tool on one side was not observed to correlate with negative topography on the other. Instead, grooves and associated gouge appeared on both sides at once. This is in

contrast to the ridge and groove-type slickensides noted by Means (1987). Necessarily, there must be a grooving agent, but it is not part of the hard rock measured by the profilometer and imaged by the photographs. As will be elaborated on below, detached gouge particles thus form a natural candidate for the grooving agent.

3.2. The Length of Grooves

While the majority of mapped features have $L < 42$ mm, many prominent grooves had length $L > 42$ mm and were thus longer than the total possible offset between the two blocks (42 mm) (one example is shown in Figure 3). As discussed in section 2, over the complete history of the apparatus, the system has been reset multiple times (supporting information Table S1), and the total cumulative slip between the blocks is ~ 140 mm. Figure 4 shows the full distribution of length L of mapped grooves and smears. Approximately 25% are more than 42 mm but only 0.5% are longer than 90 mm. Nearly all mapped features had L less than the cumulative amount of ~ 140 mm. Therefore, the total cumulative slip is limiting the size of the grooves rather than the maximum offset between the blocks.

3.3. Normal Stress and Grooves

The maps of Figure 2 show significant variability in wear as a function of distance in the slip direction (x direction) but little variability in wear in the direction perpendicular to slip (z direction). Groove density was highest at the ends and least in the middle of the block. There is also an asymmetry to the wear; groove density is highest on the leading edge.

These wear patterns and the forcing/leading edge asymmetry are particularly interesting in light of the normal stress measurements taken during previous experiments on the same apparatus (Ke et al., 2018). Direct shear experiments of this type produce higher normal stress near the fault ends than in the center, due to an edge effect (Kammer et al., 2015; Xu et al., 2019), and the asymmetry of normal stress is the result of a net moment introduced during the loading. This along-fault normal stress distribution remains relatively constant despite variations due to different loading procedures from one experiment to another (Ke et al., 2018).

Figure 5 shows that the number of mapped grooves on profiles perpendicular to slip increases with normal stress. The asymmetry of wear noted above relates to a corresponding asymmetry of normal stress based both on the eight measurement locations and from a finite element model. In particular, there was more wear at about $x = 2.7$ m, which is near the leading edge, than at the analogous position of $x = 0.4$ m, near the forcing end. The measured normal stress and the groove density are linearly correlated with an R^2 of 0.96, which corresponds to a p value of < 0.0005 for eight data points.

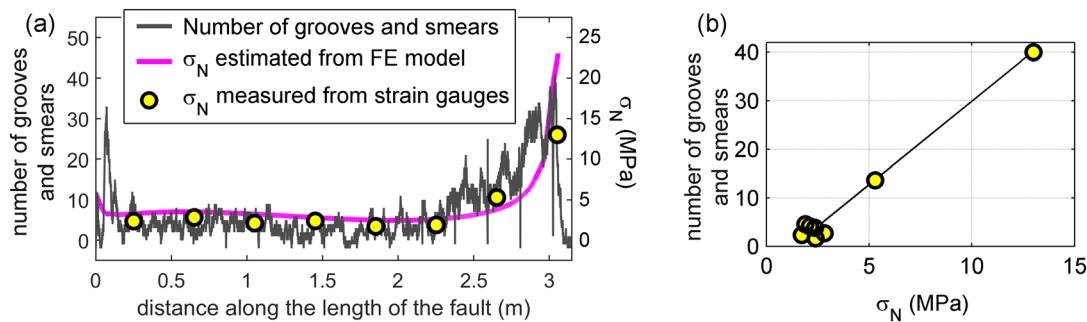


Figure 5. The number of mapped features and normal stress along the length of the fault. (a) Normal stress was measured at eight locations (yellow circles) and estimated with a finite element model (magenta line) (Ke et al., 2018) and compared to the number of mapped features (grooves and smears) in the z direction. (b) The number of grooves increased approximately linearly with measured normal stress which suggests groove density $\rho_{\text{grooves}} = 10$ grooves/m/MPa (see text).

3.4. Evidence of Gouge

Light colored fault gouge was distributed in a thin layer (a few microns thick) all over the fault surfaces; however, gouge was observed to coat and spill out from the grooves (Figure 3), consistent with previous laboratory observations (Boneh et al., 2014; Togo et al., 2015; Yamashita et al., 2015). There was a heavy coating of gouge (~ 100 μm thick) at the higher stressed fault ends. Under a microscope (Nikon Eclipse L200N 2.5X to 100X magnification), we found the majority of the gouge particles were 1 μm in size or smaller, though some larger rock flakes sampled from fault were up to 100 μm in size.

3.5. The Width of Grooves

Using the photographs and profilometer measurements we determined the width of the mapped grooves were 0.1 to 2 mm wide (Figures 2 and 3). This is far larger than most gouge particles (~ 1 μm) and similar to the grain size of the granite. Barre Gray granite has a grain size that ranges from 0.25 mm to 3 mm with average grain size 0.84 mm (Xia et al., 2008). The groove width does not appear to change systematically across the sample. Normal stress increases do not appear to change the groove width, unlike groove density. Many grooves were narrower on one side, which we refer to as the head, and appear to widen and deteriorate with continued fault slip, as gouge is transported in the z direction (perpendicular to the slip direction), similar to previous observations (Doblas, 1998; Togo et al., 2015; Yamashita et al., 2015). For example, the groove shown in Figures 3b and 3d on the moving block is narrower on the right side ($+x$ direction), and has a wider tail with gouge smeared out in the z direction on the left side of the photo. Its mirror image counterpart in Figure 3a should have its head on the left side ($-x$ direction); however, resetting of the blocks muddies this observation.

This head and tail of individual grooves is also depicted schematically in Figure 8 (right side) and can be used in this case to determine the sense of fault motion: The head observed on one fault face points in that face's direction of motion relative to the opposite face.

3.6. Grooving Regimes

On the leading edge of the sample, the grooves become denser and ultimately coalesce into a rough surface with more significant topography, lacking individual grooves. This transition can be seen in the profilometer data (Figure 6). Most of the profiles have minimal long-wavelength topography, a feature common to artificially ground surfaces (e.g., Marone & Cox, 1994). The bottom profile shows the most wear and is closest to the leading edge of the sample; the grooves have merged and are no longer distinct. This profile also has enhanced long-wavelength topography, which illustrates how coalescence of grooves can reintroduce the long-wavelength topography expected for self-affine surfaces.

There is also a hint in the data of regular spacing of the grooves in the z direction (normal to the sliding direction) in the region near the leading edge before the fully coalesced regime. We measure the spacing between the grooves for each column of the digitized map in Figure 2 and then study their distribution by measuring the mean and standard deviation in each column. We then compute the coefficient of variation by normalizing the standard deviation by the mean. Again, this measurement is done on each column individually.

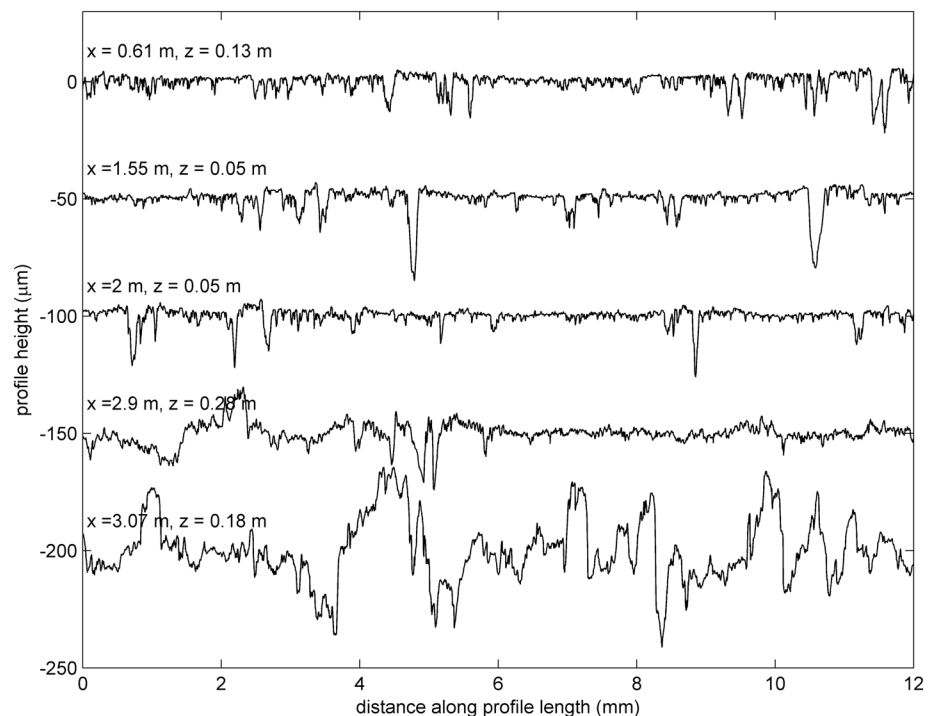


Figure 6. Surface topography and overall roughening. Representative surface topography measurements made with the stylus profilometer (Mitutoyo Surftest SJ-210 profilometer) at five locations along the 3 m granite/granite fault, offset for clarity. The x locations are marked with blue triangles in Figure 2c and labeled. The z locations report the distance from the bottom of the sample. All profiles are made in the z direction (perpendicular to the sliding direction). Profiles from the central part of the fault ($0.5 \text{ m} < x < 2 \text{ m}$) show flat-topped surfaces with occasional troughs and minor grooves. Profiles closer to the leading edge of the fault ($x = 2.9 \text{ m}$, $x = 3.07 \text{ m}$) show a progressive roughening with an increase in long-wavelength roughness. Profiles that specifically target a large groove are reported in Figures 3c and 3d.

The coefficient of variation can be used to evaluate periodicity. A value of the coefficient of variation below 1 means that the variability is low relative to the mean spacing. The limit of a coefficient of variation of 0 implies perfectly periodic behavior. Figure 7 shows that between $x = 2.3$ and 2.6 m the coefficient of variation has a modal value near 1, but beyond 2.6 m it is skewed lower. The low values imply more regular spacing in the highly stressed region.

4. Interpretations

To summarize, the key observations are (1) grooves match between opposite sides of the fault, (2) groove lengths range from 10–80 mm, which includes a range more than the maximum offset between the two surfaces before a reset and less than the cumulative fault displacement, (3) groove density increases with normal stress, but not groove width, (4) gouge is observed to spill out from grooves, (5) groove width is larger than powder particle size and similar to the grain size in the granite, (6) at sufficiently high density, grooves merge to create enhanced long-wavelength topography and may be organized into a preferred spacing at intermediate density.

4.1. Third-Body Wear

The clearest conclusion that arises from this work is the importance of gouge in creating the topography of faults. In tribology, a wear particle that is separate from the two rubbing surfaces is referred to as a third body (e.g., Godet, 1984). Godet (1984) note that the third body can be either filling the space between the other two surfaces or serving as a strut separating them. Recent work applied this third-body concept to wear of rocks during frictional sliding, and suggested that continued wear occurs at the gouge wall rock interface and that friction may coevolve with wear with the most extreme effects seen when the third bodies form a continuous

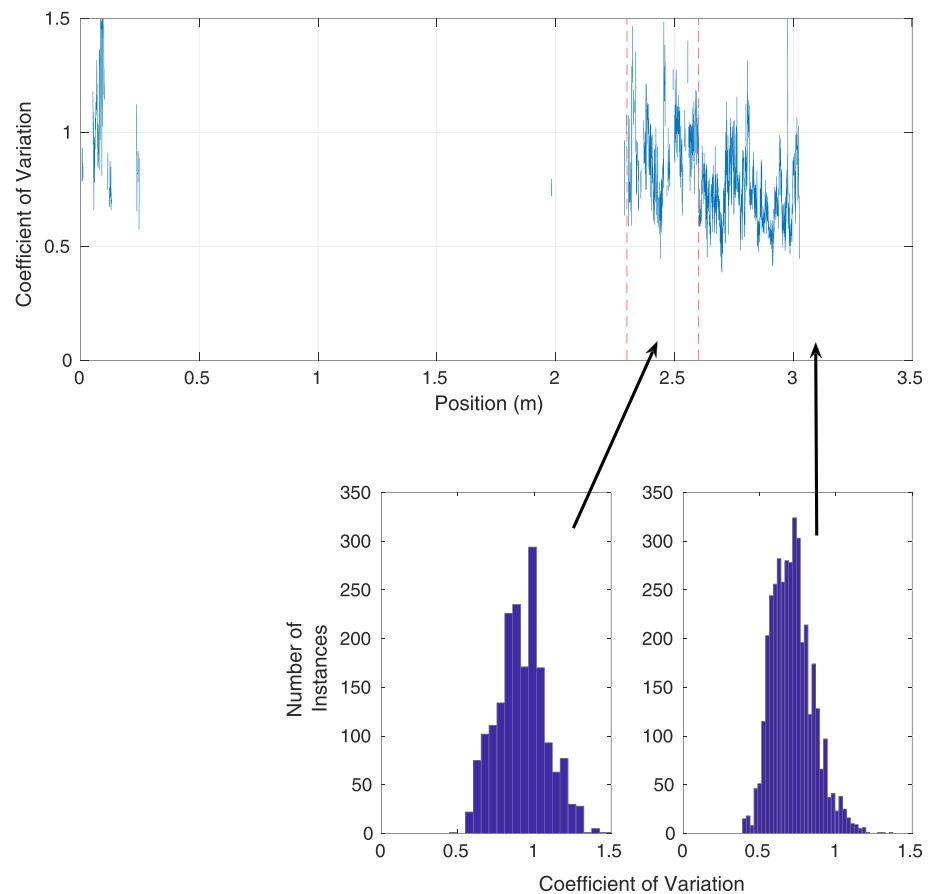


Figure 7. Groove spacing and regularity. The coefficient of variation (see text for definition) of groove spacing for each column on the image for which there is a sufficient number of grooves to form statistics. (Coefficient of variation is only measured in locations with 10 or more intergroove intervals.) Bottom left is the distribution of coefficient of variations between 2.3 and 2.6 m (region bounded by red dashed lines in upper panel), and bottom right is from 2.6 m to the edge of the image, that is, in the high normal stress region. The distribution shows lower coefficients of variation, that is, less variability in spacing in the high stress region.

layer (Boneh et al., 2013, 2014; Lyakhovsky et al., 2014). The detachment process itself may involve either plastic or brittle failure, but in either case results in particles that are no longer attached to either side (Aghababaei et al., 2016; Candela & Brodsky, 2016; Chen et al., 2020). Third-body wear is particularly apt for the groove formation process seen here. If the grooves were carved by a hard protuberance stuck to one side of the fault, as typically inferred for toolmarks attributed to asperity plowing, grooves would not be symmetric on both sides of the fault (Observation 1), and groove length would not exceed the maximum fault offset (Observation 2). Instead, the match between opposite sides of the fault and the maximum length of grooves suggests that the grooves are the result of a detached clump of gouge that damages both sides of the fault. The gouge spilling from the grooves reinforces this interpretation (Observation 4). The clump of gouge is likely the comminuted remains of one or more grains that were plucked from the wall rock. The longevity of the grooves through successive slip events indicates that an isolated clump remains an effective agent of groove formation even as wear progresses. In this work, this type of third-body wear appears to be the primary agent of groove formation.

4.2. Increased Wear at High Stress

It has long been known that wear rate increases with increasing normal stress (Archard, 1953; Boneh & Reches, 2018; Wang & Scholz, 1994). Badt et al. (2016) also found that penetrative damage and roughness increased with normal stress by comparing distinct experiments at each stress. In agreement with this, we observe increased numbers of grooves and an associated increase in roughness at the ends of the fault

that experience higher normal stress. The normal stress effect is strongest on groove density. From the photos, we measured the total number of grooves in the 0.28 m (11 inches) wide map. (Note that the transparencies used for mapping are 1 inch narrower than the block, and we did not map the bottom 1 inch.) This measurement allows us to calculate a groove density, that is, the number of grooves divided by the width of the map. Figure 5b shows at the location where the strain gauge measures 13 MPa a measurement of 40 grooves, which results in a density of 140 grooves/m. Assuming that the groove density increases linearly with stress, this maximum value corresponds to about 10 grooves/m/MPa given the 140 mm of cumulative slip that has been experienced by the block.

The observation suggests a field strategy for fault zones. Geophysicists have long wondered about the normal stress distribution in situ because it can exert a first-order control on earthquake nucleation and propagation (Lay & Kanamori, 1981; Lin & Lapusta, 2018; Mai & Beroza, 2002). Grooves may provide an observational inroad into this problem. The correlation between normal stress and wear density suggests that damage could be used as an indicator of meter-scale variations in normal stress, that is, asperities. This strategy would be most effective if the strength, hardness, or wearability of the wall rock is relatively uniform. In addition, we infer that groove density should increase with depth unless other factors that were not explored in this study, such as temperature, mitigate it.

We can speculate on the physical origin of the increased groove density. Reviewer Z. Reches suggested a scenario where increasing normal stress increases the number of asperities in contact (e.g., Archard, 1953). With increasing contacts, the opportunity for breaking asperities also increases, and thus the increasing normal stress should produce an increasing number of detached particles (Chen et al., 2020). With the increase in detached third bodies, the groove density may also increase.

In the limit of high stress, the increased groove density should transition to a qualitatively different type of surface where grooves are superimposed and lose their individual identity. If grooves are each 1 mm wide, naïve extrapolation of the observed groove density of 10 grooves/m/MPa is that at approximately 100 MPa, the grooves completely fill the surface. In fact, we observe a transition in the morphology of the surface at approximately 20 MPa (Observation 6). This lower stress transition may be the result of interaction between grooves that creates coalescence when the groove separation is equal to three to four groove widths. The field prediction here is therefore that regions with sufficiently high normal stress should transition to the coalesced roughness described at the ends of the block, which is more similar to mature fault observations than the isolated grooves (Sagy & Brodsky, 2009).

4.3. The Mechanics of Groove Generation and Feedback Mechanisms

As described schematically in Figure 8, we infer that a weak grain is plucked from the wall rock and crushed into finely comminuted wear product (gouge) that is then dragged by the dislocating fault surfaces to extend the grooves (Bhushan, 2002; Renard et al., 2012; Togo et al., 2015; Wang & Scholz, 1994; Yamashita et al., 2015). Groove widths were 0.1 to 2 mm, which is similar to the grain size of the granite (Observation 5).

For wear of rocks, the gouge clump may be an especially persistent third body for the formation of grooves due to a positive feedback mechanism (Yamashita et al., 2015). Damaged and disaggregated rocks are not as well packed as intact samples; even highly compacted gouge likely has porosity (~1–4%) at least an order of magnitude larger than the intact granite (<0.1%). This increased porosity causes wear products to expand. It is commonly observed that gouge spills out from samples during rotary shear experiments on cm-sized samples (e.g., Reches & Lockner, 2010). In the groove generation process described previously, gouge spills out of grooves (Togo et al., 2015; Yamashita et al., 2015) but remains confined within the fault and can therefore act as a stress concentrator that causes further localized damage that reinforces the feedback loop. This process can cause grooves to widen. For example, Renard et al. (2012) studied groove formation on a halite sample and observed oblique fractures on the sides of grooves and a damage zone 3–4 times wider than the original groove.

However, finely comminuted gouge particles may also act to lubricate the fault, lower its coefficient of friction (Reches & Lockner, 2010), and make the fault slip more stably (described in more detail below), and these effects could potentially act to counter the above positive feedback mechanism by reducing the stress on the indenter.

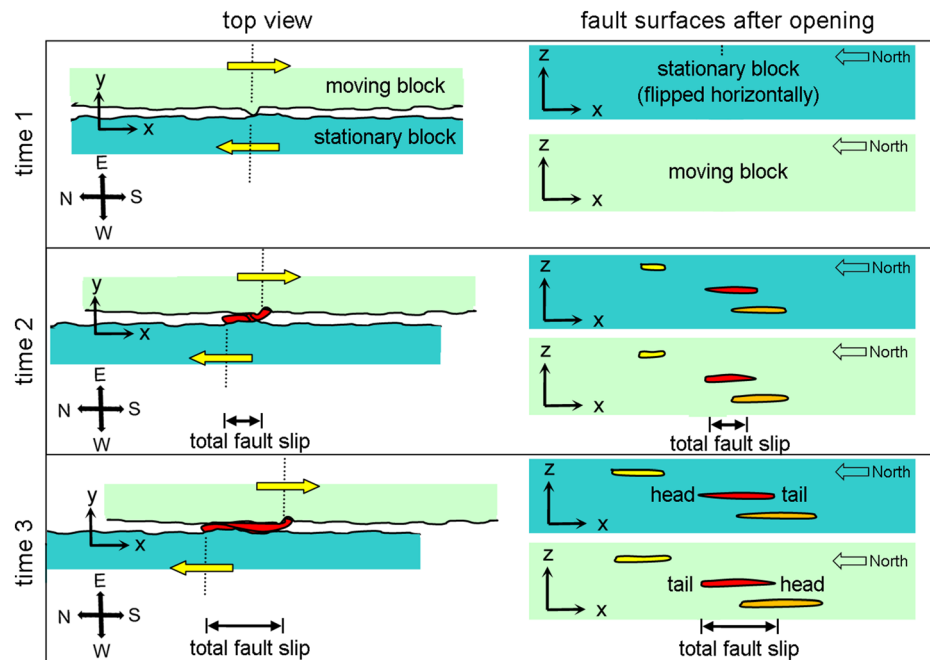


Figure 8. Cartoon of third-body wear via an isolated clump of fault gouge. The left side shows a top view of the formation of one groove. The right side shows how both fault surfaces would look if opened and reset, similar to Figure 3. Time 1: A grain or bump is plucked from the wall rock due to the interaction of surface topography. Time 2: As the fault slides, that grain is ground up into fault gouge (colored red). Other grains are plucked forming additional grooves (orange and yellow, not shown on the left side). The more porous gouge expands and acts as a stress concentrator that can cause further wear on both sides of the fault in the form of grooves. Time 3: The gouge is smeared between the two sides of the fault, and grooves are elongated. The head of the groove is where the third body first formed and is in the $+x$ direction on the moving block and $-x$ direction on the stationary block.

4.4. Fault Stability and Gouge Layer Evolution

Cumulative wear of the fault surfaces was accompanied by changes in the behavior of the 3-m sample when it was loaded. The faces of the granite samples were originally prepared by the manufacturer to be flat to $125\ \mu\text{m}$. During an initial running-in period (15 mm of cumulative slip sustained at $\sim 7\ \text{MPa}$ normal stress) the sample became stronger (sample average coefficient of friction increased from 0.5 to 0.7) and more unstable. Slip during complete-rupture dynamic slip events grew from 50 to 150–200 $\mu\text{m}/\text{event}$. This running-in process was related to the destruction of the initial topography left by the manufacturer's surface preparation: The most highly stressed contacts were crushed and ground up into gouge which helped distribute shear stress more uniformly at the mm scale. After this initial running-in period, fault properties evolved more slowly.

With continued accumulation of fault gouge, slip events became somewhat more stable and prone to creep, particularly if the sample was reset or the gouge layer was disturbed or allowed to relax without confinement. By about 80 mm of cumulative slip, the fault ends, which were highly worn, became more prone to slow aseismic creep during experiments (McLaskey, 2019). This effect was particularly strong immediately after the granite blocks were reset. In fact, experiments conducted after this mapping study was conducted were particularly prone to creep: Confined slip events had low stress drop and were not fully dynamic (see, e.g., Wu & McLaskey, 2019). When the fault gouge was subsequently wiped off both sides of the fault, we were able to readily generate fully dynamic confined slip events once again.

The increased strength and decreased stability in the running-in phase is consistent with previous work on bare rock surfaces (Togo et al., 2015) and fault gouge (Scuderi et al., 2017). In general, gouge layers are more stable than intact samples, but the propensity for creep with accumulated gouge that we observed may primarily result from disruptions to the evolving fabric of the gouge layer that occur when the fault is opened. While this disruption is less likely to occur in nature, thick gouge layers may be more prone to creep and weaken in response to stress perturbations, perhaps due to nearby earthquakes or fluid pressure variations.

4.5. Shear Fracture Energy

Shear fracture energy is a parameter thought to be important for the physics of dynamic fault rupture (Abercrombie & Rice, 2005; Nielsen et al., 2016). It has been proposed that local Mode 2 fracture energy for shear slip on a frictional interface is linearly proportional to normal stress (Bayart et al., 2015) at least over a limited stress range (1–10 MPa). This could be a result of larger true area of contact under higher normal stress (Dieterich & Kilgore, 1994).

We roughly calculate the energy consumed by the formation of the grooves and compare our measurements with previous estimates for Mode 2 fracture energy as a function of normal stress. The static Mode 1 energy release rate (Tada et al., 2000) for the granite samples $G_I^s = (K_{Ic}^s)^2/E_\infty = 33\text{--}96 \text{ J/m}^2$, where E_∞ is the static Young's modulus (30 GPa) and $K_{Ic}^s = 1.0\text{--}1.7 \text{ MPa m}^{1/2}$ (Dai & Xia, 2013) is the static Mode 1 fracture toughness of Barre Gray Granite. Using profilometer measurements as a guide (Figures 3c, 3d, and 6), we model the grooves as shallow troughs (depth of 50 μm) with diameter $d = 0.8 \text{ mm}$ equal to the average grain size (Xia et al., 2008); the energy consumed by groove formation is $dG_I^s\rho_{\text{grooves}} = 0.3\text{--}0.8 \text{ J/m}^2/\text{MPa}$, where $\rho_{\text{grooves}} = 10 \text{ grooves/m/MPa}$ (Figure 5b and section 4.2). These estimates, which should be considered a lower bound for the energy required to pluck a granite grain, are remarkably close to previous Mode 2 fracture energy estimates. Ke et al. (2018) found $0.2 \text{ J/m}^2/\text{MPa}$ (or $0.2 \mu\text{m}$) for the same granite samples, and Kammer and McLaskey (2019) estimated $0.02\text{--}0.3 \text{ J/m}^2/\text{MPa}$ from secondary rupture fronts observed on a Sierra White granite sample. Bayart et al. (2016) estimated $0.28\text{--}0.35 \text{ J/m}^2/\text{MPa}$ for samples composed of glassy polymers.

5. Conclusions

We studied the sliding surfaces of a dry granite/granite fault deformed in a 3-m-long loading machine at 1 to 20 MPa stress levels. After about 140 mm of cumulative fault slip, the fault surfaces were adorned with grooves tens of mm long and 1 mm wide. Gouge particles ($<1 \mu\text{m}$ in size) spill from the grooves. We mapped the grooves and measured profiles of the fault surface topography. We find that the grooves are the product of third-body wear: A grain of the wall rock was plucked or dislodged from a side of the fault and ground up into powder that expanded to create a stress concentration and damaged both of the fault surfaces. This results in a set of mirror image grooves on either side of the fault.

The laboratory samples had an initial topography that was unnaturally flat compared to natural faults, and this likely affected the details of our observations. However, this study shows that a dislocated and pulverized portion of a wall rock can act as tool for third-body wear, which is distinct from wear by toolmarks, and may be important for producing the grooves observed on natural faults. Rough faults in nature may be even more prone to produce third-body particles for wear as jagged edges are broken.

We find the wear patterns are strongly dependent on the local normal stress, which varies by about an order of magnitude along the length of the fault. Grooves in the low-stress central section of the fault were spaced 50 mm apart, on average. Moving closer to the highly stressed ends of the fault, groove density increased, showed a hint of a regular spacing, and then coalesced into highly worn areas with increased topography at longer wavelengths. The highly worn sample ends had thick gouge layers and were more prone to creep, particularly when the sample was reset and the fabric of the gouge was disturbed. The observations suggest a field strategy to map normal stress on exposed faults and thus address a major unknown in models of earthquake nucleation and propagation. Of course, natural faults have additional complications produced by natural roughness, heterogeneous properties, and fluid flow. It remains to be seen how effective the strategy is in nature.

Conflict of Interest

The authors declare no conflicts of interest relevant to this study.

Data Availability Statement

Data reported here are publicly available online (<https://doi.org/10.7298/j2vn-p285>).

Acknowledgments

This work was enabled by the INSTOC Jack Oliver Visiting Professorship award to E. B., and we gratefully acknowledge the opportunity. The work was also supported by NSF EAR-1624657 and NSF EAR-1763499. We thank Sara Beth L. Cebry, Bill S. Wu, Maile McCann, and Kristina Okamoto for assistance with the mapping and profilometer measurements. Reviews by Z. Reches, V. Toy, M. Kottwitz, and an anonymous reviewer improved the manuscript.

References

- Abercrombie, R. E., & Rice, J. R. (2005). Can observations of earthquake scaling constrain slip weakening? *Geophysical Journal International*, 162, 406–424. <https://doi.org/10.1111/j.1365-246X.2005.02579.x>
- Aghababaei, R., Warner, D. H., & Molinari, J.-F. (2016). Critical length scale controls adhesive wear mechanisms. *Nature Communications*, 7(1), 1, 11816–8. <https://doi.org/10.1038/ncomms11816>
- Archard, J. (1953). Contact and rubbing of flat surfaces. *Journal of Applied Physics*, 24(8), 981–988. <https://doi.org/10.1063/1.1721448>
- Badt, N., Hatzor, Y. H., Toussaint, R., & Sagy, A. (2016). Geometrical evolution of interlocked rough slip surfaces: The role of normal stress. *Earth and Planetary Science Letters*, 443, 153–161. <https://doi.org/10.1016/j.epsl.2016.03.026>
- Bayart, E., Svetlizky, I., & Fineberg, J. (2015). Fracture mechanics determine the lengths of interface ruptures that mediate frictional motion. *Nature Physics*, 12, 166–170.
- Bhushan, B. (2002). *Introduction to tribology*. New York: John Wiley & Sons.
- Boneh, Y., Chang, J. C., Lockner, D. A., & Reches, Z. (2014). Evolution of wear and friction along experimental faults. *Pure and Applied Geophysics*, 171, 3125–3141. <https://doi.org/10.1007/s00024-014-0801-3>
- Boneh, Y., & Reches, Z. E. (2018). Geotribology-friction, wear, and lubrication of faults. *Tectonophysics*, 733, 171–181. <https://doi.org/10.1016/j.tecto.2017.11.022>
- Boneh, Y., Sagy, A., & Reches, Z. (2013). Frictional strength and wear-rate of carbonate faults during high-velocity, steady-state sliding. *Earth and Planetary Science Letters*, 381, 127–137.
- Brodsky, E. E., Kirkpatrick, J. D., & Candela, T. (2016). Constraints from fault roughness on the scale-dependent strength of rocks. *Geology*, 44(1), 19–22. <https://doi.org/10.1130/G37206.1>
- Candela, T., & Brodsky, E. E. (2016). The minimum scale of grooving on faults. *Geology*, G37934.1. <https://doi.org/10.1130/G37934.1>
- Chen, X., Carpenter, B. M., & Reches, Z. (2020). Asperity failure control of stick-slip along brittle faults. *Pure and Applied Geophysics*, 177(7), 3225–3242. <https://doi.org/10.1007/s00024-020-02434-y>
- Dai, F., & Xia, K. W. (2013). Laboratory measurements of the rate dependence of the fracture toughness anisotropy of Barre granite. *International Journal of Rock Mechanics and Mining Sciences*, 60, 57–65. <https://doi.org/10.1016/j.ijrmms.2012.12.035>
- Davidesko, G., Sagy, A., & Hatzor, Y. H. (2014). Evolution of slip surface roughness through shear. *Geophysical Research Letters*, 41, 1492–1498. <https://doi.org/10.1002/2013GL058913>
- Dieterich, J., & Kilgore, B. (1994). Direct observations of frictional contacts—New insights for state-dependent properties. *Pure and Applied Geophysics*, 143, 283–302. <https://doi.org/10.1007/BF00874332>
- Doblas, M. (1998). Slickenside kinematic indicators. *Tectonophysics*, 295(1–2), 187–197. [https://doi.org/10.1016/S0040-1951\(98\)00120-6](https://doi.org/10.1016/S0040-1951(98)00120-6)
- Engelder, J. T. (1974). Cataclasis and the generation of fault gouge. *Geological Society of America Bulletin*, 85(10), 1515–1522. [https://doi.org/10.1130/0016-7606\(1974\)85<1515:CATGOF>2.0.CO;2](https://doi.org/10.1130/0016-7606(1974)85<1515:CATGOF>2.0.CO;2)
- Fondriest, M., Smith, S. A. F., Candela, T., Nielsen, S. B., Mair, K., & Toro, G. D. (2013). Mirror-like faults and power dissipation during earthquakes. *Geology*, 41(11), 1175–1178. <https://doi.org/10.1130/G34641.1>
- Godet, M. (1984). The third-body approach: A mechanical view of wear. *Wear*, 100, 437–452.
- Graham, B., Antonellini, M., & Aydin, A. (2003). Formation and growth of normal faults in carbonates within a compressive environment. *Geology*, 31(1), 11–14.
- Hirose, T., Mizoguchi, K., & Shimamoto, T. (2012). Wear processes in rocks at slow to high slip rates. *Journal of Structural Geology*, 38, 102–116. <https://doi.org/10.1016/j.jsg.2011.12.007>
- Kammer, D. S., & McLaskey, G. C. (2019). Fracture energy estimates from large-scale laboratory earthquakes. *Earth and Planetary Science Letters*, 511, 36–43.
- Kammer, D. S., Radiguet, M., Ampuero, J. P., & Molinari, J. F. (2015). Linear elastic fracture mechanics predicts the propagation distance of frictional slip. *Tribology Letters*, 57(3), 23. <https://doi.org/10.1007/s11249-014-0451-8>
- Ke, C.-Y., McLaskey, G. C., & Kammer, D. S. (2018). Rupture termination in laboratory-generated earthquakes. *Geophysical Research Letters*, 45, 12,784–12,792. <https://doi.org/10.1029/2018GL080492>
- Kirkpatrick, J. D., & Rowe, C. D. (2013). Disappearing ink: How pseudotachylites are lost from the rock record. *Journal of Structural Geology*, 52(1), 183–198. <https://doi.org/10.1016/j.jsg.2013.03.003>
- Lay, T., & Kanamori, H. (1981). Reprinted from earthquake prediction—An international review Maurice Ewing Series 4 Copyright © 1981 by the American Geophysical Union. *Earthquake Prediction - An International Review*.
- Lin, Y., & Lapusta, N. (2018). Microseismicity simulated on asperity-like fault patches: On scaling of seismic moment with duration and seismological estimates of stress drops. *Geophysical Research Letters*, 45, 8145–8155. <https://doi.org/10.1029/2018GL078650>
- Lyakhovsky, V., Sagy, A., Boneh, Y., & Reches, Z. E. (2014). Fault wear by damage evolution during steady-state slip. *Pure and Applied Geophysics*, 1–15.
- Mai, P. M., & Beroza, G. C. (2002). A spatial random field model to characterize complexity in earthquake slip. *Journal of Geophysical Research*, 107(B11), 2308. <https://doi.org/10.1029/2001JB000588>
- Marone, C., & Cox, S. J. D. (1994). Scaling of rock friction constitutive parameters: The effects of surface roughness and cumulative offset on friction of gabbro. *Pure and Applied Geophysics*, 143(1–3), 359–385. <https://doi.org/10.1007/BF00874335>
- McLaskey, G. C. (2019). Earthquake initiation from laboratory observations and implications for foreshocks. *Journal of Geophysical Research: Solid Earth*, 124, 12,882–12,904. <https://doi.org/10.1029/2019JB018363>
- Means, W. D. (1987). A newly recognized type of slickenside striation. *Journal of Structural Geology*, 9, 585–590.
- Nielsen, S., Spagnuolo, E., Smith, S. A. F., Violay, M., Di Toro, G., & Bistacchi, A. (2016). Scaling in natural and laboratory earthquakes. *Geophysical Research Letters*, 43, 1504–1510. <https://doi.org/10.1002/2015GL067490>
- Reches, Z., & Lockner, D. A. (2010). Fault weakening and earthquake instability by powder lubrication. *Nature*, 467, 452–455.
- Renard, F., Mair, K., & Gundersen, O. (2012). Surface roughness evolution on experimentally simulated faults. *Journal of Structural Geology*, 45, 101–112.
- Rowe, C. D., & Griffith, W. A. (2015). Do faults preserve a record of seismic slip: A second opinion. *Journal of Structural Geology*, 78, 1–26. <https://doi.org/10.1016/j.jsg.2015.06.006>
- Sagy, A., & Brodsky, E. E. (2009). Geometric and rheological asperities in an exposed fault zone. *Journal of Geophysical Research*, 114, B02301. <https://doi.org/10.1029/2008JB005701>
- Scuderi, M. M., Colletini, C., Viti, C., Tinti, E., & Marone, C. (2017). Evolution of shear fabric in granular fault gouge from stable sliding to stick slip and implications for fault slip mode. *Geology*, 45(8), 731–734.

- Tada, H., Paris, P. C., & Irwin, G. R. (2000). *The stress analysis of cracks handbook edited by 3*. Three Park Avenue New York, NY 10016–5,990: ASME.
- Tisato, N., Di Toro, G., De Rossi, N., Quaresimin, M., & Candela, T. (2012). Experimental investigation of flash weakening in limestone. *Journal of Structural Geology*, 38, 183–199. <https://doi.org/10.1016/j.jsg.2011.11.017>
- Togo, T., Shimamoto, T., Yamashita, F., Fukuyama, E., Mizoguchi, K., & Urata, Y. (2015). *Earthquake Science*, 28, 97–118. <https://doi.org/10.1007/s11589-015-0113-4>
- Toy, V. G., Niemeijer, A., Renard, F., Morales, L., & Wirth, R. (2017). Striation and slickenline development on quartz fault surfaces at crustal conditions: Origin and effect on friction: Striae, Slickenlines, and Fault Strength. *Journal of Geophysical Research: Solid Earth*, 122, 3497–3512. <https://doi.org/10.1002/2016JB013498>
- Wang, W., & Scholz, C. H. (1994). Wear processes during frictional sliding of rock: A theoretical and experimental study. *Journal of Geophysical Research*, 99, 6789–6799. <https://doi.org/10.1029/93JB02875>
- Wu, B. S., & McLaskey, G. C. (2019). Contained laboratory earthquakes ranging from slow to fast. *Journal of Geophysical Research: Solid Earth*, 124, 10,270–10,291. <https://doi.org/10.1029/2019JB017865>
- Xia, K., Nasser, M. H. B., Mohanty, B., Lu, F., Chen, R., & Luo, S. N. (2008). Effects of microstructures on dynamic compression of barre granite. *International Journal of Rock Mechanics and Mining Sciences*, 45, 879–887.
- Xu, S., Fukuyama, E., & Yamashita, F. (2019). Robust estimation of rupture properties at propagating front of laboratory earthquakes. *Journal of Geophysical Research: Solid Earth*, 124, 766–787. <https://doi.org/10.1029/2018JB016797>
- Yamashita, F., Fukuyama, E., Mizoguchi, K., Takizawa, S., Xu, S., & Kawakata, H. (2015). Scale dependence of rock friction at high work rate. *Nature*, 528, 254–257.